scientific reports

Check for updates

OPEN

M²DGAT: Multi-view multi-scale dynamic graph attention network(GAT) based prediction of Parkinson's disease(PD) progression using whole-blood RNA sequencing data

Zhang Wei[1]✉, Xu Zeqi[1,3], Wu Chenjun[1] & Dai Qi[2]✉

With emerging single-cell transcriptomics data, deep learning approaches have enabled the diagnosis of neurodegenerative disorders such as Parkinson's disease(PD). Based on whole-blood RNA sequencing data, the graph neural network has predicted Parkinson's disease(PD) progression trajectories by exploiting spatial and temporal views that were related with neurodegenerative disorders. The single-view learning scheme, which focuses on gene expression embedding, was still insufficient in analyzing complicated human brain diseases. As a type of spatial representation underlying transcriptomics data, gene graphs that are closely associated with disease states have been inferred to investigate regulatory mechanisms and molecular dynamics. For disease-specific gene graphs, global and local structures contribute to fine-grained spatial representations. With the dynamic graph attention network (DGAT) backbone, this study proposes a multi-view, multi-scale M² DGAT method to predict disease progression trajectories for neurodegenerative disorders. Temporal and spatial views have been integrated by the count sketch bilinear (CSB) fusion strategy. Based on RNA sequencing data from human blood samples, joint-view representations have been constructed to predict disease stages and relevant cognitive scores. Experiments about the PPMI and PDBP cohorts have validated the effectiveness and efficiency of the proposed M²DGAT architecture in disease prediction applications. The proposed M²DGAT method has demonstrated significant superiority in predictive accuracy over established cutting-edge disease prediction approaches. Compared with static graphs, dynamic graph representations tend to encode more dynamics about disease progression.

Keywords Multi-view graph learning, Whole-blood transcriptomics data, Spatiotemporal representations, Parkinson's disease(PD) progression

Prediction of disease progression for neurodegeneration has become an important topic in precision medicine. For neurodegenerative diseases such as Parkinson's disease(PD), single-cell transcriptomics data have become an important information source in precision diagnosis for neurodegenerative disorders. As RNA sequencing(RNASeq) data is highly complicated and noisy, the prediction of disease progression trajectories is usually challenged[1]. Among heterogeneous modalities, clinical metadata-based prediction generally considers condensed features of human brain diseases while ignoring deep-level dynamics about regulatory mechanisms. Compared with conventional statistical analysis approaches, deep neural networks-based disease prediction methods have provided deeper insights into the abnormal molecular mechanisms underlying transcriptomics data[2–4]. Such abnormal patterns are too subtle to be accurately detected and sufficiently exploited by conventional deep learning approaches.

[1]College of Computer Science and Technology, Zhejiang Sci-Tech University, Hangzhou 310017, China. [2]College of Life Science and Biomedicine, Zhejiang Sci-Tech University, Hangzhou 310017, China. [3]Zhejiang Mintai Commercial Bank, Hangzhou, China. ✉email: zhangweicse@zstu.edu.cn; daiqi@zstu.edu.cn

With an enhanced understanding of cellular heterogeneity, dozens of deep learning architectures have been proposed to explore high-order molecular dynamics that govern disease states[5–8]. Using genetic data, 36-month or longer progression trajectories of motor impairment, as described by MDS-UPDRS II and III metrics, have been predicted from a combination of demographic, clinical, genetic, and neuroimaging data. With supervised information on MDS-UPDRS scores, deep learning-based diagnostics aim to detect meaningful abnormalities in gene expression data. During computational analysis of single-cell RNASeq data, conventional machine learning methods such as multi-layer perceptron(MLP) face the problems of low prediction accuracy and reliability. In this case, graph neural networks(GNN) have exhibited superior performance in biomedical data mining. More importantly, the GNN schemes are highly compatible with spatial representations underlying whole-blood RNA sequencing data. Such structural features are associated with topological changes of gene networks as well as cell graphs, that govern information flow at the molecular level.

Recent studies in PD transcriptomics indicate that disease-associated genes tend to aggregate into co-expression modules and regulatory subgraphs whose topology correlates with clinical phenotypes and pathological burden, suggesting that network structure itself carries important biological and prognostic information[9,10]. The longitudinal analysis of blood-based transcriptomics data validates the positive role of gene networks in disease prediction. Spatial representations of gene graphs have encoded regulatory mechanisms about the disease onset, progression, as well as molecular heterogeneity[11,12]. In line with these findings, dual-view graph learning frameworks that explicitly encode Parkinson-specific gene graphs as spatial representations in subtype detection. Based on whole-blood transcriptomics data, the joint learning of temporal expression embeddings and spatial representations is able to boost the accuracy and reliability in PD progression prediction[13].

From the temporal view, temporal expression embeddings underlying RNASeq data have been widely applied to explore biologically meaningful patterns about neurodegeneration, by focusing in temporal changes of gene expression levels. Transformer and non-transformer architectures, namely graph attention network, have been employed to investigate abnormal expression patterns, with the purpose of disease prediction. Due to limited power, single-view learning schemes face the problem of low accuracy and poor generalization capability in precision diagnosis of human brain disease[14]. Molecular system dynamics, including early-onset and late-onset disease stages, have exhibited subtle while crucial difference in transcript levels as well as topological changes of gene networks[15–17]. This phenomenon suggests that integrating gene expression levels and gene networks is a feasible and effective solution to obtain reliable prediction models in brain disease diagnosis. To investigate high-order dynamics underlying whole-blood transcriptomics data, dynamic graph learning schemes have emerged as a powerful architecture to investigate spatiotemporal representations. Moreover, multi-scale spatial representations of gene networks tend to be more expressive than global structure[18,19].

Instead of single-view temporal expression embeddings, the proposed M^{2}DGAT method aims to investigate spatiotemporal dynamics underlying whole-blood transcriptomics data, thus predicting disease progression for neurodegenerative disorders. From the perspective of motor as well non-motor dysfunction, disease progression trajectories have been predicted by a dual-view graph learning algorithm. The contributions of this M^{2}DGAT method have been summarized as follows:

- Under the framework of multi-view learning, the spatiotemporal representations of whole-blood RNA sequencing data have been constructed to predict short-term motor and non-motor dysfunction;
- For whole-blood transcriptomics data, the local and global structure features of PD-GN have been integrated to construct fine-grained spatial representations in the precision diagnosis of neurodegenerative disorders;
- Based on the backbone of dynamic GAT, the proposed M^{2}DGAT method has adopted a dual-view learning scheme to predict disease progression dynamics, with the spatiotemporal representations determined by the CSB fusion strategy.

Graph learning based PD progression prediction

In this work, the problem of disease prediction refers to the identification of PD stages using multi-omics data, by investigating meaningful features about neurodegenerative disorders. Whole-blood RNA sequencing data contain rich cellular information that captures disease dynamics[20–22]. Biologically meaningful representations have been extracted to explore spatiotemporal changes associated with disease stages. In order to obtain reliable diagnostic outcomes, PD-specific gene networks have been employed as spatial representations in decision-making about disease states.

Multi-view multi-scale dynamic graph attention network(M^{2}DGAT)

Inspired by spatiotemporal graph learning technique[23–29], the proposed M^{2}DGAT architecture, aims to explore biologically meaningful spatial representations of evolving gene graphs. Using whole-blood transcriptomics data, the PD progression has been quantitatively investigated from the viewpoint of motor and non-motor dysfunction, respectively.

The framework of M^{2}DGAT is demonstrated in Fig. 1, which contains four essential blocks. These blocks are responsible for multi-scale graph learning, the extraction of evolving gene graphs, dynamic GAT, and count sketch bilinear (CSB) fusion block, respectively.

In Fig. 1, the CSB fusion strategy has obtained joint-view representations that were more expressive than those obtained by the direct concatenation strategy. Subsequently, structural changes of PD-specific gene graphs(PD-GN) have been systematically investigated.

Multi-scale graph learning

For whole-blood transcriptomics data, the gene count matrix X at each snapshot contains m patients and each patient has n genes. To obtain valuable spatial representations, disease-specific gene co-expression network(PD-

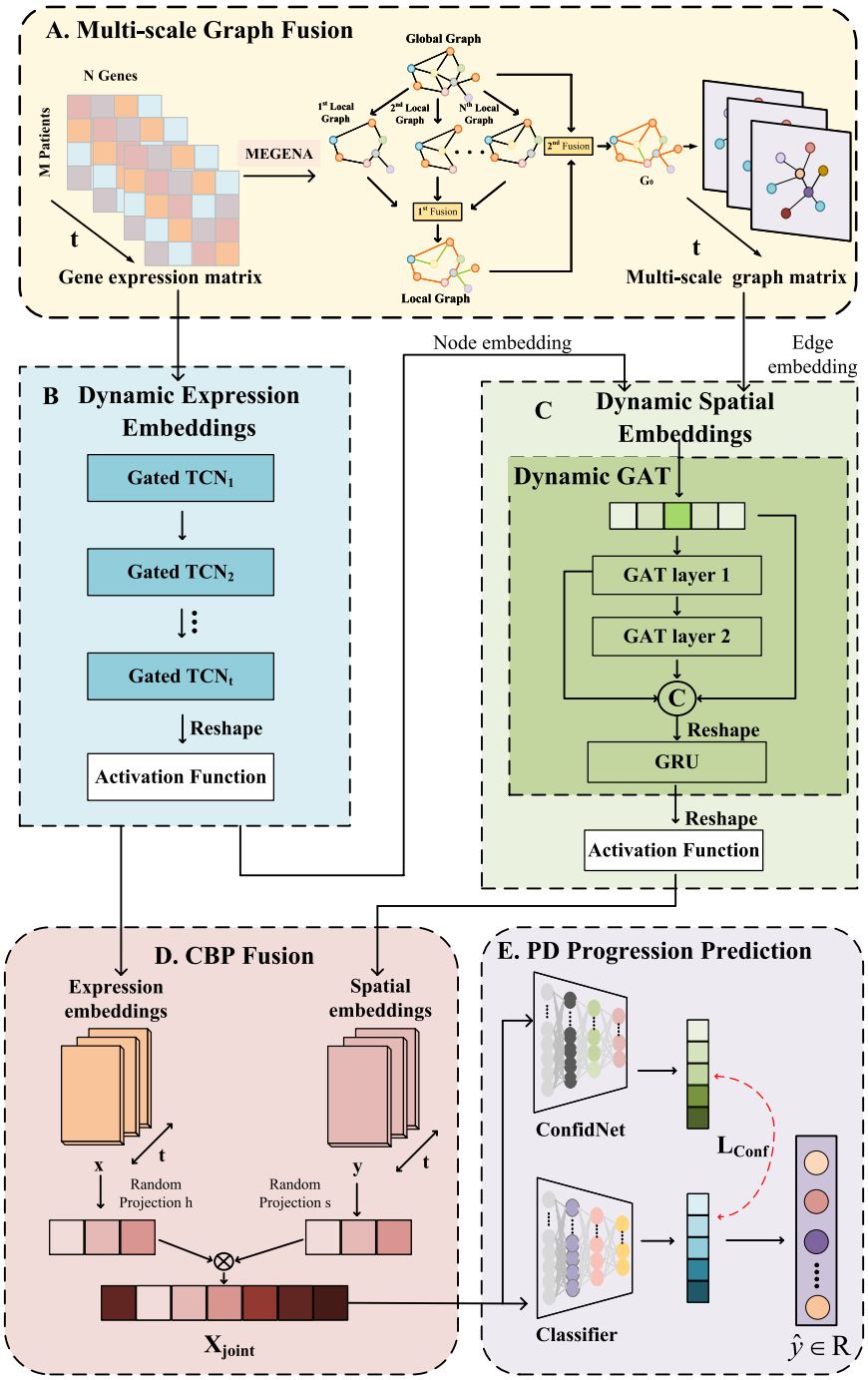

Fig. 1. Overview of the M^{2}DGAT method. The MEGENA algorithm was employed to construct multiscale gene co-expression networks, which were subsequently fused into a unified multi-scale graph for each snapshot. (B) A gated TCN block was employed to extract temporal-view specific embeddings from time-varying node features. (C) For dynamic gene graphs, the dynamic GAT backbone analyzed evolving spatial representations through stacked GAT layers and a GRU element. (D) In order to determine spatiotemporal dynamics, the Count Sketch Bilinear (CSB) fusion combines temporal and spatial views. (E) Joint-view representations have been obtained for conduct disease progression prediction with relevant confidence intervals.

GN) were inferred using the MEGENA algorithm[30,31]. In order to investigate regulatory mechanisms, inferred PD-GNs were exploited as spatial representations to explore structural changes of gene networks.

Prior to computing gene–gene correlations, this work performed data preprocessing on the gene count matrix at each snapshot to ensure comparability across patients and to reduce technical artifacts. Expression values were transformed onto a consistent scale and normalized across samples before the Pearson correlation matrices were

calculated. Batch effects were assessed using low-dimensional projections and, when present, were corrected at the expression-matrix level prior to network inference. The resulting preprocessed expression matrix was used as the input for subsequent correlation computation and MEGENA-based multiscale graph construction.

Specifically, the Pearson correlation coefficients were first used to determine the correlation matrix between gene pairs, as described by Eq (1).

$$r_{ij} = \frac{\sum_{k=1}^{m}(x_{ik} - \overline{x}_i)(x_{jk} - \overline{x}_j)}{\sqrt{\sum_{k=1}^{m}(x_{ik} - \overline{x}_i)^2 \sum_{k=1}^{m}(x_{jk} - \overline{x}_j)^2}} \tag{1}$$

For gene *i* and *j*, the corresponding expression profiles across the *m* patients were denoted as $(x_{i1}, x_{i2}, \ldots, x_{im})$ and $(x_{j1}, x_{j2}, \ldots, x_{jm})$, respectively. $\overline{x}_i$ and $\overline{x}_j$ are the corresponding average expression levels. To enhance both computational tractability and network robustness, we incorporate several implementation refinements during the construction of the global co-expression network $G^{(0)}_{\text{coexp}}(V, E)$. First, the computation of the correlation matrix is parallelized by dividing gene–gene comparisons into independent blocks that are distributed across multiple CPU cores. This block-wise concurrency has substantially reduced the computational complexity associated with high-dimensional transcriptomic data.

In addition, an early-termination criterion has been implemented during correlation calculation. When the partial covariance accumulation indicates that the eventual absolute correlation cannot surpass a predefined significance threshold, the computation for that gene pair is halted. The pruning mechanism eliminates unnecessary operations for weakly related genes, thereby accelerating network inference. Subsequently, a set of upstream quality-control procedures has been applied prior to correlation computation. These steps mitigate technical noise and reduce the risk of spurious correlations propagating into the downstream multiscale clustering analysis.

Following the construction of $G^{(0)}_{\text{coexp}}$, multi-scale clustering analysis (MCA) is performed to identify hierarchical gene regulatory modules. During the MCA operation, regulatory module at each resolution are obtained by maximizing the modular compactness score Q_s with respect to the module assignments. For each candidate resolution parameter γ, the algorithm searches for the partition that maximizes Q_s, and therefore yields a distinct regulatory structure at scale *s*. The modular compactness of the MCA mechanism was formulated by Eq. (2).

$$Q_s = \sum_i \left(\frac{|E_i^{in}|}{|E_i^{total}|} \right)^{\gamma} \tag{2}$$

where $|E_i^{in}|$ represents the number of edges within regulatory module *i*, $|E_i^{total}|$ represents the total number of edges in the module, and γ is the resolution parameter.

For blood transcriptomics data, global and local structural information reflect two topological levels about disease-specific gene graphs. Spatial representations at the local and global scales were integrated, thus obtaining augmented representations[9,32–34].

Multi-scale graph learning aims to integrate the global and local structure of gene graphs associated with neurodegenerative disorders[34]. Specifically, the local structure refers to the distributions of regulatory modules $G^s(s = 1, 2, ..S)$ within gene co-expression network, where *S* denotes the number of graphs. The number of scales *S* was determined by sampling the resolution parameter γ over a logarithmic grid and evaluating the stability of module assignments under perturbation-based resampling. These scales with stable partitions with the consensus > 85% have been retained, yielding a multi-scale representations. Each subgraph G^s shares the same node set as the global co-expression network $G^{(0)}_{\text{coexp}}$, but differs in the edge structure induced by the resolution parameter at the scale *s*.

After the clustering, each subgraph was collapsed into a super-node to form a coarse-grained graph representation. Intra-module edges were aggregated into weighted self-loops to preserve the internal regulatory strength of modules while reducing graph complexity. This results in a scale-dependent, structurally consistent set of regulatory graphs that capture different levels of granularity. Gene co-expression network $G^{(0)}_{\text{coexp}}$ corresponds to the global structure in subsequent graph learning. Preliminary fusion is conducted to capture the local structure according to Eq (3).

$$\overline{G} = \sum_{s=1}^{S} a_s G^s \tag{3}$$

In Eq (3), a_s denotes the weight matrix, which is used to unite multiple combinations of local maps. In this study, a_s is defined as a *scalar* weighting coefficient rather than a matrix. Each scalar a_s regulates the contribution of the corresponding scale-specific adjacency matrix G^s. Since multi-scale graphs share the same ordered node set and were represented as compatible adjacency matrices, the scalar weighting was sufficient for linear fusion and avoids parameter inflation.

Here, each graph G^s was formulated as an adjacency matrix defined on the same ordered gene set. Therefore, the summation in Eq. (10) constitutes a linear combination of structurally aligned edge-weight matrices, rather than an operation on node-feature representations, thereby ensuring the algebraic soundness of the fusion. Local structure $\overline{G}$ was integrated with the global structure of gene graphs, described by Eq (4).

$$G_0 = \eta \overline{G} + (1 - \eta) G^{(0)}_{\text{coexp}} \tag{4}$$

where G_0 represents the embedding obtained by multi-scale graph learning, and η denotes the weight matrix that integrates the local and global structures. The hyperparameter η was defined as a *scalar* in the interval [0, 1], which controls the balance between the local structure $\overline{G}$ and the global network $G^{(0)}_{\mathrm{coexp}}$. Both $\overline{G}$ and $G^{(0)}_{\mathrm{coexp}}$ were adjacency matrices with identical dimensionality, scalar interpolation enables element-wise fusion without requiring matrix-valued weights. For the PD-GN, the consensus and complementary components between the local and global structure have been integrated.

Extraction of evolving gene graphs

During disease progression, both graph-structured data and node features were temporal evolving due to the increasing level of system disorder. Changes of gene expression levels were regarded as temporal embeddings. To investigate the causal interactions, this work has incorporated a gated temporal convolutional mechanism in analyzing evolving gene graphs. Gated TCN was employed to capture variations in gene expression levels through dilated convolutions along the temporal dimension.

Conventional TCNs enlarge the temporal receptive field through dilated convolutions but lack the ability to selectively regulate which temporal signals should be propagated or suppressed. Blood transcriptomic trajectories exhibit considerable noise and heterogeneous fluctuations across patients, making selective control of temporal information flow particularly important. The gating mechanism therefore provides an explicit means to retain biologically meaningful long-range dependencies while attenuating irrelevant or noisy variations.

This design is particularly advantageous in dynamic gene expression embedding, where only a subset of temporal features contributes to disease progression and must therefore be emphasized selectively. Compared with conventional TCN[35], the gated TCN block aims to control the flow of information within the network, making it suitable for involving time-series sequences. The gating mechanism has enhanced the ability to capture long-range dependencies while addressing issues such as overfitting and vanishing gradients. For the input feature *X* of dynamic graph nodes, the gated TCN is formulated as follows:

$$\begin{aligned} &TCN_{\phi}(X) = Conv_g(X) \\ &GateTCN(X) = \tanh(TCN_{\phi_1}(X)) \odot \sigma(TCN_{\phi_2}(X)) \end{aligned} \tag{5}$$

In Eq (5), $Conv_g(X)$ represents the dilated convolution along the temporal dimension, while $TCN_{\phi_1}(X)$ and $TCN_{\phi_2}(X)$ have different parameters, ϕ_1 and ϕ_2, respectively. $\tanh$ and σ are activation functions. This selective gating allows the model to preserve informative temporal patterns and prevents gradient dilution during deep temporal stacking, leading to more robust temporal embeddings for downstream spatial–temporal fusion.

Dynamic GAT backbone

Compared with static graph-structured data, evolving gene graphs were employed to gain deep insights about regulatory abnormality, especially about information flows that govern disease progression dynamics. In this case, the dynamic graph learning architecture is capable of dealing with evolving gene graphs as well as temporal expression embeddings of RNASeq data. Overview of dynamic GAT is demonstrated by Fig. 2.

In Fig. 2, the GRU block in the DGAT backbone analyzes evolving gene graphs. Each individual corresponds to a unique gene graph $G_0 = (X_t, E_t)$ that encodes multi-scale spatial representations about whole-blood transcriptomics data. The symbols X_t and E_t represent the gene count matrix and the edge matrix at the time snapshot *t*, respectively. In addition, multi-scale graph G_0 was applied to construct fine-grained spatial representations of gene graphs. The output of each graph level was defined by Eq. (6).

$$h_i' = \Big\|_{k=1}^{K} \sigma\left(\sum_{j \in N_i} \alpha_{ij}^{(\mathrm{att}),k} W^k h_j\right) \tag{6}$$

In Eq (6), *K* denotes the *k*-th layer, *W* is the weight matrix, σ represents the nonlinear activation function. N_i denotes first-order neighbor nodes of node *i*, the element $\alpha_{ij}^{(\mathrm{att})}$ corresponds to learnable attention coefficients, which are described by Eq (7).

$$\alpha_{ij}^{(\mathrm{att})} = \frac{\exp\left(\mathrm{LeakyReLU}\left(a_{\mathrm{att}}^T [Wh_i \,\|\, Wh_j]\right)\right)}{\sum_{k \in N_i} \exp\left(\mathrm{LeakyReLU}\left(a_{\mathrm{att}}^T [Wh_i \,\|\, Wh_k]\right)\right)} \tag{7}$$

where LeakyReLU denotes a nonlinear activation function, a_{att} refers to the learnable weight vector, and $\|$ represents a cascade operation. As G_0 passes through the first GAT layer, it was aggregated into G_1, which acts as a high-level graph, to obtain G_2. The outputs of the two-layer GAT are concatenated to obtain a more discriminative spatial representation *G*.

$$G = \mathrm{Concat}\left[G_{\mathrm{gat}}^{(0)}, G_{\mathrm{gat}}^{(1)}, G_{\mathrm{gat}}^{(2)}\right] \tag{8}$$

Evolutionary dynamics and structural distortions of disease-specific gene graphs were jointly analyzed by updating network parameters of dynamic GAT model with the GRU mechanism. The updating process of embeddings in the dynamic GAT backbone was formulated by Eq. (9).

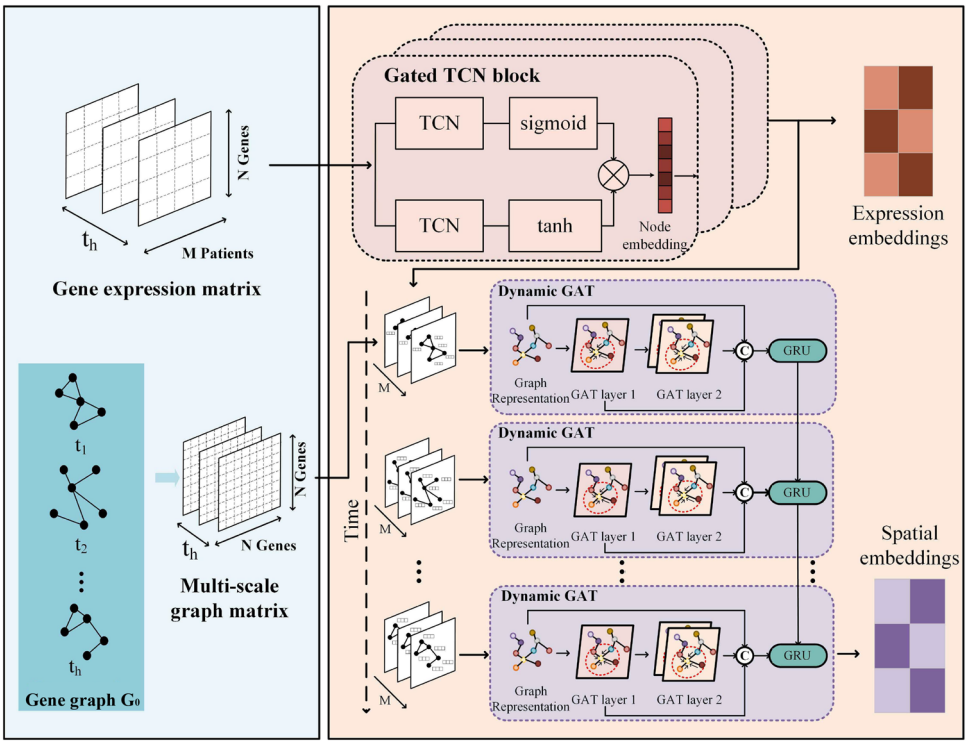

Fig. 2. The architecture of the dynamic GAT block and the gated TCN block embedded in the M^{2}DGAT method. Feature tensors were constructed to capture gene expression changes and adjacency tensors were employed to investigate structural distortion of PD-GN. Evolving PD-GNs at multiple snapshots have been compressed to investigate biologically meaningful regulatory mechanisms that govern PD progression dynamics.

$$\begin{aligned} z_t &= \sigma(x_t W_Z + U_Z h_{t-1}) \\ r_t &= \sigma(x_t W_r + U_r h_{t-1}) \\ \tilde{h}_t &= tanh(x_t W_x + U_h(r_t \cdot h_{t-1})) \\ h_t &= (1 - z_t)h_{t-1} + z_t \cdot \tilde{h}_t \end{aligned} \tag{9}$$

where x_t act as the input vector of t-th snapshot, $W_z, W_r, W_x, U_Z, U_r, U_h$ are the learnable weight matrices. $h_{(t-1)}$ preserves the structural information of the past snapshot $t-1$, and σ denotes nonlinear activation function. Temporal expression vector x_t was transformed linearly to update gates z_t and reset gate r_t. In this case, temporal expression embeddings were preserved as $\tilde{h}_t$ through the reset gate. Ultimately, the objective function of STGAT takes the form of cross-entropy, defined by Eq (10).

$$L_{DGAT}^{(t)} = -\frac{1}{NT}\sum_{i=1}^{N}\sum_{t=1}^{T}\sum_{c=1}^{C} y_{i,t,c}\log\left(\widehat{y}_{i,t,c}\right) + \lambda\sum_{j}\|\theta_j\|^2 \tag{10}$$

where N and T denote the number of patients and snapshots respectively, $y_{i,t,c}$ is the supervised information about the disease category c, while $\widehat{y}_{i,t,c}$ is the predicted probability of the i-th sample at snapshot t. Regularization term $\lambda\sum_j \|\theta_j\|^2$ was adopted to keep a balance between two penalty terms.

Count sketch bilinear (CSB) fusion strategy

Joint-view representation of whole-blood RNA sequencing data was constructed by capturing high-order dynamics underlying whole-blood RNA sequencing data. Using bilinear pooling strategy[36], joint-view representations have been obtained by computing the outer product of spatial representations and temporal embeddings, shown by Eq (11).

$$B(x, y) = x \cdot W \cdot y \tag{11}$$

where x and y are temporal and spatial views respectively, while W is the weight matrix and B denotes joint-view representations.

Regarding high computational and storage costs of conventional bilinear pooling, the work proposes a Count Sketch based Bilinear Pooling (CSB) strategy, which uses random projection to approximate the outer product of bilinear pooling. Specifically, two hash functions, *h* and *s*, are defined as follows:

$$\begin{aligned} h_x,\ s_x : \{1, 2, \ldots, m\} \rightarrow \{1, 2, \ldots, d\} \\ h_y,\ s_y : \{1, 2, \ldots, n\} \rightarrow \{-1, +1\} \end{aligned} \tag{12}$$

where *h*, *s* are used to map feature indices to a lower-dimensional space, *d* represents the dimension of low dimensional space. Therefore, the count sketches for *x* and *y* are denoted as Z_x and Z_y, with the definitions shown by Eq. (13).

$$\begin{aligned} Z_x(k) &= \sum_{i=1}^{m} x_i \cdot s_x(i) \cdot \mathbb{I}(h_x(i) = k) \\ Z_y(k) &= \sum_{j=1}^{n} y_j \cdot s_y(j) \cdot \mathbb{I}(h_y(j) = k) \end{aligned} \tag{13}$$

where m and n represent the dimensions of the original temporal expression embeddings and spatial representation, respectively, the symbols x_i and y_j denote the *i*-th element of vector *x* and the *j*-th element of vector *y*, respectively. $s_x(i)$ is the random sign corresponding to $x_i \in (-1, 1)$, was used for sign flipping. $\mathbb{I}(h_x(i) = k)$ and $\mathbb{I}(h_y(j) = k)$ are indicator functions. If $h_x(i) = k$ or $h_y(j) = k$, the value of the indicator function is 1; otherwise, it is 0. Joint-view representations were computed as follows:

$$X_{joint} = Z_x \odot Z_y \tag{14}$$

To handle the problem of overestimation, the confidence criteria was used to assign confidence levels to predicted probability distributions[37]. At the *t*-th snapshot, a confidence neural network with parameter $\theta^{(t)}$ is applied to estimate confidence interval on the training set. The objective function of confidential network is defined as follows:

$$L_{Conf}^{(t)} = \|P(Y = y^{(t)}|X^{(t)}) - \widehat{P}(Y = \theta^{(t)}|X^{(t)})\|^2 \tag{15}$$

Ultimately, the total loss of the M^{2}DGAT model is defined by Eq.(16).

$$L = L_{DGAT}^{(t)} + L_{Conf}^{(t)} \tag{16}$$

The penalty term $L_{Conf}^{(t)}$ constructs the confidence neural network for each snapshot and generates the confidence scores after receiving the feature representations from the GRU block.

Experimental outcomes and analysis

The M^{2}DGAT model contains three major blocks, i.e. the dynamic GAT backbone, multi-scale graph(MSG) learning and the CSB block. To evaluate the feasibility and effectiveness of the proposed M^{2}DGAT framework, comparative experiments have been conducted with state-of-the-art methods on the PPMI[38] and PDBP[39] cohorts.

Datasets and implementation settings

During the prediction of PD progression, whole-blood transcriptomics data were employed to analyze the motor and non-motor dysfunction. The specific details are shown in Table 1. As the training sets, blood transcriptomics data from the Parkinson's Disease Progression Marker Initiative (PPMI) and Parkinson's Disease Biomarker Program (PDBP) cohorts were downloaded from the Accelerated Medicines Partnership Parkinson's Disease (AMP-PD) platforms. Multi-view Transformer(MvT) network has been trained on an Nvidia GeForce RTX 4090 GPU and optimized using the Adam optimizer. The initial learning rate is set to 0.0001 and decays to 80% of its current value every 100 epochs to accelerate the convergence of the objective function. During training, the batch size was set as 32.

Task	Supervision	Dataset	Patients	Temporal snapshots
Motor dysfunction	The H&Y stages	PPMI	278	M6,M12,M18,M24
		PDBP	358	M6,M12,M24,M36
Non-motor dysfunction	MoCA score	PPMI	187	M0,M12,M24,M36
		PDBP	385	M0,M12,M24,M36

Table 1. Descriptions of whole-blood transcriptomics datasets from the PPMI and PDBP platforms. In order to explore the molecular dynamics of Parkinson diseases, RNASeq datasets from human blood samples have been collected.

Performance comparison of the M^{2}DGAT method and candidate disease prediction approaches has been conducted on the PPMI and PDBP cohorts. The Hoehn & Yahr (H&Y) stages and Montreal Cognitive Assessment (MoCA) scores were employed as supervised information in the prediction of motor and non-motor dysfunction. In two types of subtasks, the number of genes and nodes was settled as 58780 and 500, respectively. Detailed descriptions about experimental datasets were given in Table 1.

In Table 1, the five-stages Hoehn & Yahr (H&Y) system for Parkinson's disease was used to assess the severity of motor impairment in patients. The Montreal Cognitive Assessment (MoCA) was a standardized tool widely used for evaluating cognitive function in patients with Parkinson's disease (PD). The MoCA system assesses multiple cognitive domains and has a range of [0,30].

For the PPMI and PDBP cohorts, the spatial and temporal views of disease-specific RNASeq data were analyzed to explore deep-level dynamics. Inherent relations between disease states and structural changes of gene graphs have been identified by dual-view graph learning. In addition, blood transcriptomics data measured in multiple snapshots provide the opportunity to investigate dynamic graph-structured data that are associated with disease states. Such dynamic spatial representations were employed to predict short-term disease progression trajectories.

Descriptions about SOTA methods

We compare the proposed M^{2}DGAT model with some state-of-the-art disease prediction approaches, as follows:

- FC-LSTM[40] : Long Short-Term Memory networks use memory cells and gating mechanisms to efficiently and accurately capture long-term and short-term dependencies in time series data.
- MvT[41]: Multi-view Transformer architecture has captured and integrated spatiotemporal relationships for time-series data by fusing representations from temporal and spatial views.
- GAT[42]: Graph Attention Networks effectively capture temporal dependencies and dynamic changes between nodes through the self-attention mechanism and dynamic edge weight learning.
- STGAT[43]: Spatial-temporal graph attention networks employed the graph attention mechanism to capture spatial dependencies in the graph sequences. The LSTM network was incorporated to extract temporal gene embeddings.
- STS-DGNN[44]: Dynamic graph neural network with spatiotemporal synchronization considers the dynamics of graph sequences and is capable of jointly extracting spatiotemporal representations.

Visualization of evolving gene graphs

Besides increased information content, evolving gene graphs tend to encode evolutionary mechanism that govern disease states. For whole-blood transcriptomics data in PPMI & PDBP cohorts, temporal expression embeddings were employed to explore temporal features, with the purpose of disease staging. In addition, spatial representations of gene graphs have encoded structural information at the molecular level, including the substructure distortions and the loss of hierarchy. Specifically, evolving gene graphs act as the input of a dynamic graph learning scheme, with the purpose of exploring biologically meaningful patterns. Evolving gene graphs at various stages were depicted by Fig. 3.

In Fig. 3, there exist multiple regulatory modules in the gene graphs, which correspond to various biological functions such as immune regulation. In general, the distributions and interactions between regulatory modules were regarded as the local structures. Furthermore, distributions of regulatory modules exhibit differences at multiple disease stages.

Under these circumstances, the DGAT model enables in-depth analysis of disease dynamics by exploring functional organizations and the hierarchy of PD-GN. For gene graphs, the local and global graph learning contribute to fine-grained analysis of spatial representations.

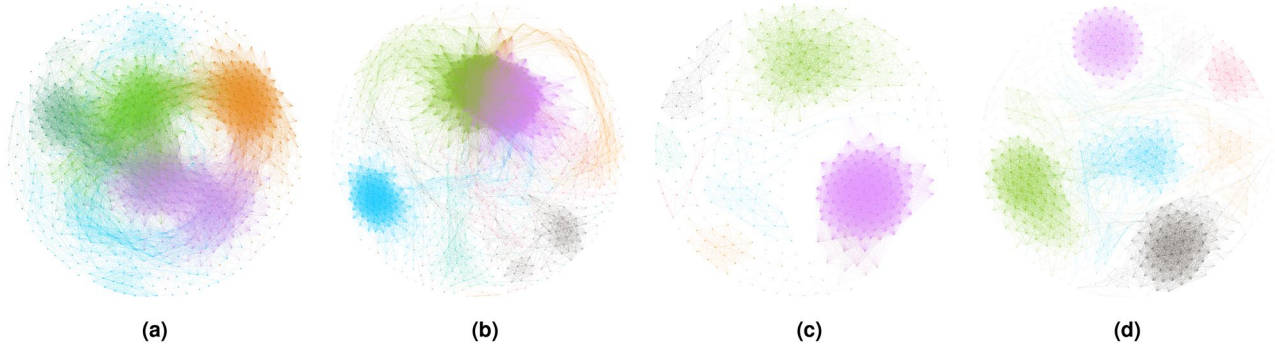

Fig. 3. Global structure of PD-specific gene graphs at multiple disease stages. These disease stages cover 6-months(M6), 12-months(M12), 18-months(M18) and 24-months(M24) after the onset of Parkinson's disease. Mapping functions between structural distortions of PD-GN and the unified Parkinson's disease rating scale have been investigated by a dynamic GAT backbone.

Performance comparison with SOTA approaches

Disease progression has been evaluated using Hoehn & Yahr (H&Y) from the perspective of non-motor dysfunction, i.e. the UPDRS-III scores. Non-motor scores also serve as supervised information in disease prediction. Specifically, graph neural networks are applied to explore abnormal patterns from whole-blood transcriptomics data.

The MvT, STGAT and STS-DGNN models have been selected as spatiotemporal graph learning approaches that exploit joint-view representations of RNASeq data[41,43,44]. Among these multi-view graph learning architectures, the STGAT and STS-DGNN schemes have been proposed to predict traffic flows. Comparisons of multiple deep learning-based prediction methods have been conducted on the PPMI and PDBP cohorts, as shown in Table 2.

In Table. 2, the STGAT and STS-DGNN approaches have obtained superior accuracy than the GAT backbone that applies the single-view learning scheme. With joint-view representations, the multi-view learning architectures could explore deep-level regulatory dynamics that govern disease states. Such joint-view representations, which were extracted from blood transcriptomics data by the CSB fusion strategy, were highly useful by exploiting cross-view interactions between temporal and spatial views.

It is noted that deep learning approaches including multi-view Transformer(MvT) and GAT, outperform the FC-LSTM backbone. This phenomenon indicates that deep learning methods are more powerful in extracting disease-specific patterns from RNASeq data. In the schemes that use static features, the GAT backbone obtained even slightly more accurate predictions than the MvT architecture, indicating that incorporating graph-based representations may further benefit predicting Parkinson's disease (PD) progression trajectories.

Multi-view learning approaches including MvT, STGAT[43], STS-DGNN[44] and the proposed M^{2}DGAT method have been compared. In order to demonstrate the effectiveness of the CSB fusion, the corresponding ROC curves in disease prediction have been compared in Fig. 4.

Established multi-view learning architectures, including STGAT and STS-DGNN, have demonstrated the feasibility and computational efficiency in integrating spatial and temporal views of RNASeq data. Evaluation metrics obtained by M^{2}DGAT validate the advantages of the CSB fusion strategy, indicating that joint-view representations contain increased information content than that obtained by direct concatenation and cascade strategies.

During the prediction of non-motor scores, the estimation errors obtained by the STS-DGNN, STGAT, MvT and the proposed M^{2}DGAT method were compared, as illustrated in Fig. 5. Both STS-DGNN and STGAT were employed as spatiotemporal graph learning architectures to conduct multi-view learning. In the comparison, the mean absolute error (MAE) and root mean squared error (RMSE) metrics were recorded to evaluate the prediction accuracy in disease progression prediction.

In Fig. 5, the proposed M^{2}DGAT method has dramatically reduced estimation errors in predicting non-motor scores from RNASeq data, demonstrating its superior performance than the conventional spatiotemporal graph learning methods.

Ablation study

To further validate the contributions of various blocks, this section has conducted an ablation study for the proposed M^{2}DGAT framework, including multi-scale graph learning, dynamic GAT backbone, and the CSB fusion module. Ablation experiments were conducted on the motor-PPMI and motor-PDBP subtasks, with detailed evaluation metrics demonstrated in Table 3.

In Table 3, the cooperation of three blocks, i.e., the MSG block, the dynamic GAT backbone, and the CSB fusion strategy, is highly effective in investigating spatiotemporal dynamics underlying RNA sequencing data. For disease modeling, the M^{2}DGAT method has significantly enhanced the accuracy in predicting motor and non-motor dysfunction. From the perspective of evaluation metrics, the contribution of the CSB block to the prediction accuracy was obvious. With joint-view representations obtained by the CSB block, the spatial and temporal views of whole-blood transcriptomics data have been efficiently integrated.

Datasets	Model	ACC	F1	Recall	Precision
PPMI	FC-LSTM[40]	0.666 ± 0.017	0.547 ± 0.011	0.672 ± 0.018	0.460 ± 0.012
	MvT[41]	0.671 ± 0.019	0.550 ± 0.008	0.674 ± 0.008	0.459 ± 0.005
	GAT[42]	0.683 ± 0.007	0.564 ± 0.007	0.681 ± 0.011	0.544 ± 0.002
	STGAT[43]	0.691 ± 0.008	0.589 ± 0.012	0.689 ± 0.009	0.588 ± 0.016
	STS-DGNN[44]	0.688 ± 0.007	0.594 ± 0.011	0.699 ± 0.012	0.579 ± 0.009
	M^{2}DGAT	**0.743 ± 0.012**	**0.704 ± 0.014**	**0.740 ± 0.018**	**0.776 ± 0.025**
PDBP	FC-LSTM[40]	0.629 ± 0.018	0.504 ± 0.004	0.601 ± 0.018	0.410 ± 0.037
	MvT[41]	0.644 ± 0.006	0.511 ± 0.006	0.635 ± 0.006	0.455 ± 0.024
	GAT[42]	0.664 ± 0.006	0.508 ± 0.010	0.640 ± 0.006	0.439 ± 0.025
	STGAT[43]	0.689 ± 0.009	0.555 ± 0.016	0.682 ± 0.012	0.548 ± 0.016
	STS-DGNN[44]	0.683 ± 0.007	0.564 ± 0.007	0.681 ± 0.011	0.544 ± 0.005
	M^{2}DGAT	**0.735 ± 0.011**	**0.595 ± 0.016**	**0.698 ± 0.022**	**0.744 ± 0.039**

Table 2. Comparison of evaluation metrics obtained by M^{2}DGAT and candidate disease prediction methods.

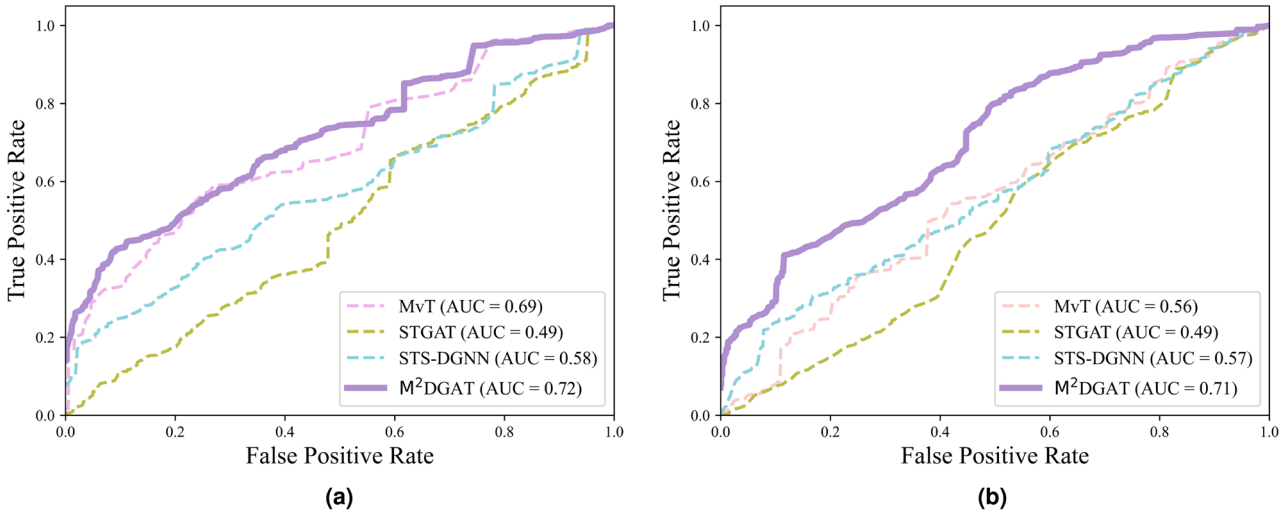

Fig. 4. Performance comparison of M²DGAT with direct concatenation fusion strategy. During integrating temporal and spatial views, the CSB fusion strategy has obtained superior performance than direct concatenation in predicting PD progression.

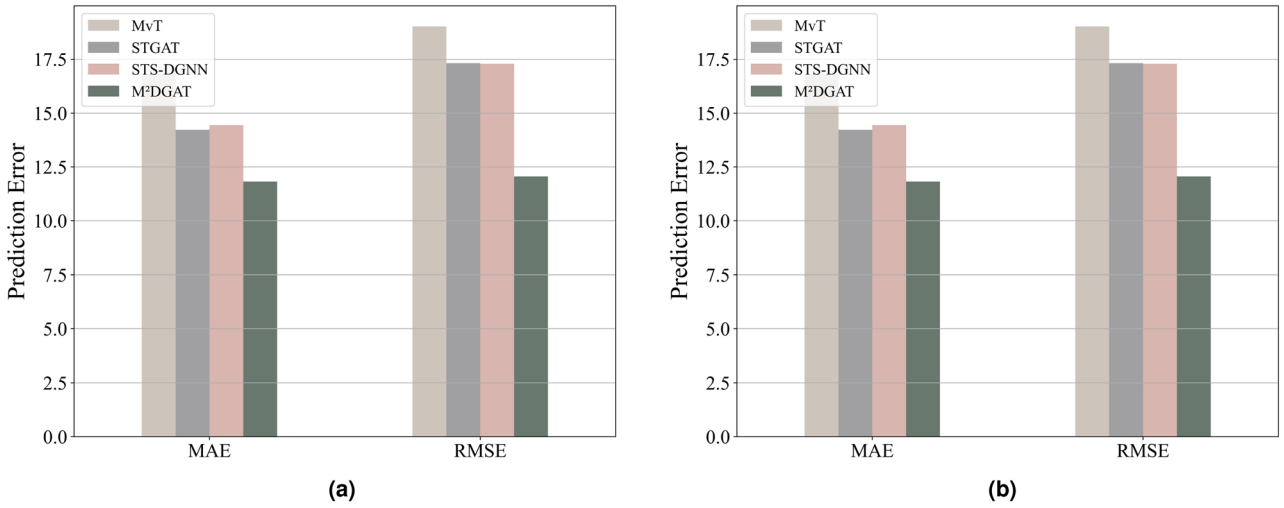

Fig. 5. Prediction errors obtained by the M²DGAT method and SOTA methods in predicting non-motor dysfunction caused by neurodegenerative disorders. Spatiotemporal representations underlying blood transcriptomics data were used to assess the degree of cognitive impairment that was associated with PD.

DGAT	MSG	CSB	PPMI				PDBP			
			Acc	F1	Recall	Precision	Acc	F1	Recall	Precision
			0.683±0.022	0.564±0.018	0.681±0.027	0.544±0.019	0.644±0.030	0.508±0.023	0.640±0.028	0.439±0.021
✓			0.694±0.019	0.616±0.021	0.688±0.026	0.629±0.018	0.654±0.034	0.528±0.025	0.653±0.031	0.635±0.024
✓	✓		0.705±0.024	0.633±0.020	0.715±0.032	0.647±0.017	0.668±0.029	0.546±0.022	0.665±0.030	0.682±0.026
✓	✓	✓	**0.743± 0.012**	**0.704± 0.014**	**0.740±0.018**	**0.776±0.025**	**0.735±0.011**	**0.595±0.016**	**0.698±0.022**	**0.744±0.039**

Table 3. Ablation study about three blocks in M²DGAT. The columns 'MSG' and 'CSB' correspond to the multi-scale graph learning and count sketch bilinear fusion strategy, respectively.

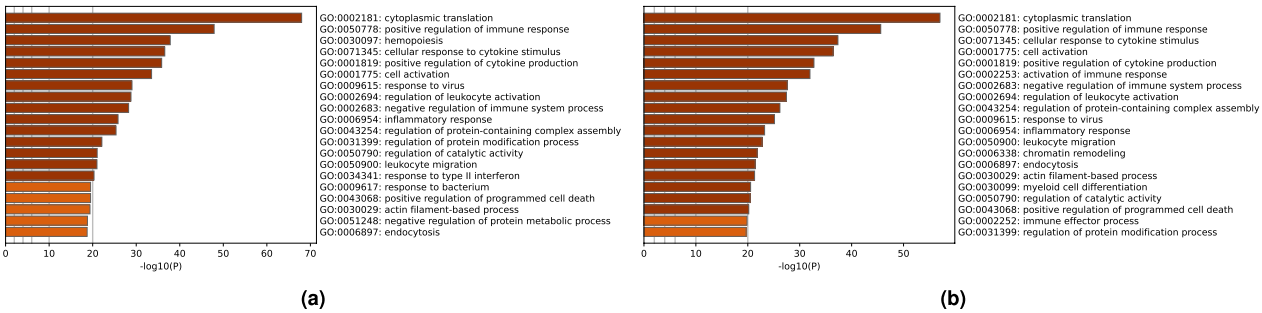

Fig. 6. Gene Ontology(GO) enrichment analysis of the selected genes at the M6 snapshot for PDBP (a) and PPMI (b). Key enriched pathways involve cytoplasmic translation, immune activation, cytokine signaling, and cell-death–related processes. The consistent patterns across the PPMI and PDBP cohorts support the biological relevance of the identified PD-associated gene signatures.

Gene ontology enrichment analysis

To further elucidate the biological relevance of the key genes identified by our model, this study conducted Gene Ontology (GO) biological process enrichment analysis for both PDBP and PPMI cohorts at the M6 snapshot. Both PPMI and PDBP benchmark datasets have exhibited highly consistent enrichment outcomes. This indicates that the proposed M^{2}DGAT method captures stable and biologically meaningful mechanisms underlying PD progression across independent cohorts.

In both PDBP-M6 and PPMI-M6 snapshots, the most significantly enriched pathway was cytoplasmic translation (GO:0002181), which was closely related to dysregulation of protein synthesis machinery. This finding aligns with recent evidence that impaired translational control contributes to proteostasis disruption and facilitates the accumulation of misfolded proteins such as α-synuclein in Parkinson's disease. For two cohorts, gene ontology analysis about crucial modules has been depicted in Fig. 6.

As demonstrated by Fig. 6, another enriched ontology involved immune function and inflammatory processes, including positive regulation of immune response, activation of immune response, cytokine production, leukocyte activation, and inflammatory response. These pathways reflect both peripheral and central immune activation, a hallmark of PD pathology. The consistent enrichment across datasets indicates that our model robustly identifies gene signatures associated with chronic inflammation and immune dysregulation in Parkinson's disease.

In addition, the signal pathways such as cell activation, programmed cell death, chromatin remodeling, regulation of catalytic activity, and endocytosis were also enriched. These processes were closely associated with neuronal vulnerability, transcriptional dysregulation, and defective intracellular trafficking, further supporting the biological plausibility of identified regulatory modules.

For disease-specific genes, the enrichment analysis demonstrates that the model captures biologically interpretable patterns involving proteostasis imbalance, immune activation, and cell-death–related pathways—mechanisms that are widely implicated in PD progression. High concordance between the PDBP and PPMI benchmarks provides strong cross-cohort evidence for the robustness of the proposed M^{2}DGAT framework.

Discussion

For whole-blood transcriptomics data about brain diseases, dynamic graph attention networks (DGAT) were used as backbone to analyze evolving gene graphs, aiming to explore structural disorders of regulatory networks. Gene graphs are useful in disease classification and diagnosis. Dynamic gene graphs tend to be more informative and expressive. Experimental analysis about the AMP-PD benchmark datasets indicated that evolving gene graphs played a positive role in improving prediction performance in disease prediction, due to increased information content of representations. More importantly, the functional interactions between disease-specific genes have been revealed more thoroughly by dynamic graph learning.

Unlike conventional expression patterns, spatial representations underlying blood transcriptomics data can analyze regulatory relations between risk genes that govern the progression of neurodegenerative disorders. Based on blood transcriptomics data, spatial representations were analyzed from the global and local scales, to investigate structural changes of disease-specific gene graphs. For disease-specific gene graphs, regulatory modules acted as local topology, while gene networks correspond to the global structures. Under the framework of graph learning-based disease prediction, these two types of structural features were complementary to each other to a certain degree. In this case, multi-scale graph learning has been employed to construct multi-scale spatial representations by integrating local-global structures.

By integrating both global and local structural information, the disease diagnostic model's performance was significantly improved by the multi-scale spatial representations. This phenomenon suggests that multi-scale gene graphs tend to encode high-order regulatory dynamics about complex gene-wise interactions, compared with the global structure. As fine-grained spatial representations, local structures were hypothesized to determine the flow and exchange of information within regulatory network. For the proposed M^{2}DGAT method, the primary function of the MSG block is to obtain graph representations that effectively capture structural distortions at the level of gene graphs.

Using transcriptomics data as training sets, experimental results suggest that combining multi-scale structural features with dynamic temporal embeddings provides joint representations that are more informative about disease-relevant regulatory mechanisms and cellular dynamics. The proposed M^2DGAT framework has extended existing network-based approaches by capturing both multi-scale spatial representations and temporal expression embeddings, thereby outperforming single-view learning approaches. These findings are consistent with recent studies emphasizing the importance of transcriptomic network architecture in neurodegenerative disorders. With dynamic graph-structured representations, the positive value of multi-scale graph learning paradigms was highlighted for network-level analysis of Parkinson's disease.

By focusing on spatiotemporal representations underlying RNA sequencing data, the proposed M^2DGAT method has adopted the CSB fusion strategy to take cross-view interactions into account. The primary function of the CSB fusion is to effectively integrate spatial and temporal views to obtain joint-view representations, including motor and non-motor dysfunction in disease progression. In the dual-view graph learning architecture, the spatiotemporal representations seem to be compatible with the CSB fusion strategy to gain a deep insight into the regulatory mechanisms of brain diseases.

Additionally, this study further investigated the impact of the CSB module on the performance of dual-view graph learning approach. Experimental outcomes indicate that the M^2DGAT method, which adopts a dual-view learning approach, outperforms the single-view learning architecture that applies the expression embeddings. This phenomenon suggests that incorporating a spatiotemporal representations of transcriptomics data enables the investigation of high-order regulatory dynamics, thereby enhancing the model's predictive accuracy and interpretability.

Data availability

The Parkinson's Progression Markers Initiative (PPMI, http://www.ppmi-info.org/) and the Parkinson's Disease Biomarkers Program (PDBP, https://pdbp.ninds.nih.gov/) benchmarks used in this study were both accessible through the AMP-PD platform (https://amp-pd.org/). To access clinical and omics data at the AMP-PD Tier 2 level, users are required to complete the data use agreement (DUA) document and submit an online application.

Code availability

The source code for the proposed method is available at https://github.com/ZJ-BMDmining/M2DGAT.

Received: 28 February 2025; Accepted: 13 February 2026
Published online: 02 March 2026

References

1. Makarious, M. B. et al. Multi-modality machine learning predicting Parkinson's disease. *npj Park. Dis.* **8**, 35 (2022).
2. Sadaei, H. J. et al. Genetically-informed prediction of short-term Parkinson's disease progression. *npj Park. Dis.* **8**, 143 (2022).
3. Kamath, T. et al. Single-cell genomic profiling of human dopamine neurons identifies a population that selectively degenerates in Parkinson's disease. *Nat. neuroscience* **25**, 588–595 (2022).
4. Fernandes, H. J. et al. Single-cell transcriptomics of Parkinson's disease human *in vitro* models reveals dopamine neuron-specific stress responses. *Cell Rep.* https://doi.org/10.1016/j.celrep.2020.108263 (2020).
5. Song, C., Teng, Y., Zhu, Y., Wei, S. & Wu, B. Dynamic graph neural network for fake news detection. *Neurocomputing* **505**, 362–374 (2022).
6. Zhang, M., Wu, S., Yu, X., Liu, Q. & Wang, L. Dynamic graph neural networks for sequential recommendation. *IEEE Trans. Knowl. Data Eng.* **35**, 4741–4753 (2022).
7. Zhu, Y. et al. Wingnn: dynamic graph neural networks with random gradient aggregation window. In *Proceedings of the 29th ACM SIGKDD Conference on Knowledge Discovery and Data Mining*, 3650–3662 (2023).
8. Sun, B., Zhao, D., Shi, X. & He, Y. Modeling global spatial-temporal graph attention network for traffic prediction. *IEEE Access* **9**, 8581–8594 (2021).
9. Wang, Q. et al. The landscape of multiscale transcriptomic networks and key regulators in Parkinson's disease. *Nat. communications* **10**, 5234 (2019).
10. D'Angiolini, S., Lui, M., Mazzon, E. & Calabrò, M. Network analysis performed on transcriptomes of Parkinson's disease patients reveals dysfunction in protein translation. *Int. J. Mol. Sci.* **25**, 1299 (2024).
11. Valentine, M. N. et al. Multi-year whole-blood transcriptome data for the study of onset and progression of parkinson's disease. *Sci. Data* **6**, 20 (2019).
12. Chew, G. et al. Transcriptomic imputation of genetic risk variants uncovers novel whole-blood biomarkers of parkinson's disease. *NPJ Parkinsons Dis.* **10**, 99 (2024).
13. Zhang, W., Xu, Z., Yu, R., Jiang, M. & Dai, Q. Dualgcn-ge: integration of spatiotemporal representations from whole-blood expression data with dual-view graph convolution network to identify parkinson's disease subtypes. *BMC Bioinformatics* **26**, 208 (2025).
14. Zhou, C. et al. Two distinct trajectories of clinical and neurodegeneration events in parkinson's disease. *NPJ Parkinsons Dis.* **9**, 111 (2023).
15. Billingsley, K., Bandres-Ciga, S., Saez-Atienzar, S. & Singleton, A. Genetic risk factors in parkinson's disease. *Cell Tissue Res.* **373**, 9–20 (2018).
16. Tasaki, S. et al. Multiomic disease signatures converge to cytotoxic cd8 t cells in primary sjögren's syndrome. *Ann. Rheum. Dis.* **76**, 1458–1466 (2017).
17. Smajić, S. et al. Single-cell sequencing of human midbrain reveals glial activation and a parkinson-specific neuronal state. *Brain* **145**, 964–978 (2022).
18. Li, M. M., Huang, K. & Zitnik, M. Graph representation learning in biomedicine and healthcare. *Nat. Biomed. Eng.* **6**, 1353–1369 (2022).
19. Yan, H. et al. Prior knowledge-guided multilevel graph neural network for tumor risk prediction and interpretation via multi-omics data integration. *Brief. Bioinform.* **25**, bbae184 (2024).
20. Craig, D. W. et al. RNA sequencing of whole blood reveals early alterations in immune cells and gene expression in Parkinson's disease. *Nat. Aging* **1**, 734–747 (2021).
21. Irmady, K. et al. Blood transcriptomic signatures associated with molecular changes in the brain and clinical outcomes in Parkinson's disease. *Nat. Commun.* **14**, 3956 (2023).

22. Kern, F. et al. Deep sequencing of sncrnas reveals hallmarks and regulatory modules of the transcriptome during Parkinson's disease progression. *Nat. Aging* **1**, 309–322 (2021).
23. Liu, J., Xu, C., Yin, C., Wu, W. & Song, Y. K-core based temporal graph convolutional network for dynamic graphs. *IEEE Trans. Knowl. Data Eng.* **34**, 3841–3853 (2020).
24. Sun, Y. et al. Dual dynamic spatial-temporal graph convolution network for traffic prediction. *IEEE Trans. Intell. Transp. Syst.* **23**, 23680–23693 (2022).
25. Pareja, A. et al. Evolvegcn: Evolving graph convolutional networks for dynamic graphs. *In Proceedings of the AAAI conference on artificial intelligence* **34**, 5363–5370 (2020).
26. Yi, K. et al. Fouriergnn: Rethinking multivariate time series forecasting from a pure graph perspective. *Adv. Neural Inf. Process. Syst.* **36**, (2024).
27. Lei, K., Qin, M., Bai, B., Zhang, G. & Yang, M. Gcn-gan: A non-linear temporal link prediction model for weighted dynamic networks. In *IEEE INFOCOM 2019-IEEE conference on computer communications*, 388–396 (IEEE, 2019).
28. Wang, C., Zhang, H., Yao, S., Yu, W. & Ye, M. Mdgcn: Multiple graph convolutional network based on the differential calculation for passenger flow forecasting in urban rail transit. *J. Adv. Transp.* **2021**, 1–10 (2021).
29. Song, C., Lin, Y., Guo, S. & Wan, H. Spatial-temporal synchronous graph convolutional networks: A new framework for spatial-temporal network data forecasting. *In Proceedings of the AAAI conference on artificial intelligence* **34**, 914–921 (2020).
30. Langfelder, P. & Horvath, S. Wgcna: An r package for weighted correlation network analysis. *BMC Bioinformatics* **9**, 1–13 (2008).
31. Song, W.-M. & Zhang, B. Multiscale embedded gene co-expression network analysis. *PLoS Comput. Biol.* **11**, e1004574 (2015).
32. Jiang, K. et al. Multi-scale progressive fusion network for single image deraining. In *Proceedings of the IEEE/CVF conference on computer vision and pattern recognition*, 8346–8355 (2020).
33. Godinez, W. J., Hossain, I., Lazic, S. E., Davies, J. W. & Zhang, X. A multi-scale convolutional neural network for phenotyping high-content cellular images. *Bioinformatics* **33**, 2010–2019 (2017).
34. Zhang, Z., Guan, J. & Zhou, S. Fragat: A fragment-oriented multi-scale graph attention model for molecular property prediction. *Bioinformatics* **37**, 2981–2987 (2021).
35. Hewage, P. et al. Temporal convolutional neural (tcn) network for an effective weather forecasting using time-series data from the local weather station. *Soft Comput* **24**, 16453–16482 (2020).
36. Lin, T.-Y., RoyChowdhury, A. & Maji, S. Bilinear cnn models for fine-grained visual recognition. In *Proceedings of the IEEE international conference on computer vision*, 1449–1457 (2015).
37. Corbière, C., Thome, N., Bar-Hen, A., Cord, M. & Pérez, P. Addressing failure prediction by learning model confidence. *Adv. Neural Inf. Process. Syst.* **32**, (2019).
38. Marek, K. et al. The parkinson progression marker initiative (ppmi). *Prog. neurobiology* **95**, 629–635 (2011).
39. Sharma, S. et al. Biomarkers in parkinson's disease (recent update). *Neurochem. Int.* **63**, 201–229 (2013).
40. Karim, F., Majumdar, S., Darabi, H. & Chen, S. Lstm fully convolutional networks for time series classification. *IEEE Access* **6**, 1662–1669 (2017).
41. Li, S. et al. Enhancing the locality and breaking the memory bottleneck of transformer on time series forecasting. *Adv. neural information processing systems* **32,** (2019).
42. Veličković, P. et al. Graph attention networks. arXiv preprint arXiv:1710.10903 (2017).
43. Zhang, C., James, J. & Liu, Y. Spatial-temporal graph attention networks: A deep learning approach for traffic forecasting. *IEEE Access* **7**, 166246–166256 (2019).
44. Li, F.-J., Zhang, C.-Y. & Chen, C. P. Sts-dgnn: Vehicle trajectory prediction via dynamic graph neural network with spatial-temporal synchronization. *IEEE Trans. Instrum. Meas.* https://doi.org/10.1109/TIM.2023.3307179 (2023).

Acknowledgements

This work is sponsored by Natural Science Foundation of Zhejiang Province, China (LQ24F030007), National Natural Science Foundation of China (62302455, 62172369), and National Key Research and Development Program of China (2023YFF1205000).

Author contributions

Zhang W: Conceptualization, methodology, data analysis, and writing the original draft. Xu Z, Wu C: Data collection, validation, and interpretation of experimental results. Zhang W, Wu C: Literature review, modifying the manuscript. Dai Q: Supervision, project administration.

Declarations

Competing interests

The authors declare no competing interests.

Ethics approval

Approval was obtained from the Ethics Committee of the Zhejiang Sci-Tech University. The authors confirm that experimental analysis was performed in accordance with relevant guidelines and regulations.

Additional information

Supplementary Information The online version contains supplementary material available at https://doi.org/10.1038/s41598-026-40636-x.

Correspondence and requests for materials should be addressed to Z.W. or D.Q.